Journal of Microscopy, Vol. 214, Pt 3 June 2004, pp. 297–314
Received 22 July 2003; accepted 12 November 2003

Robust incremental compensation of the light attenuation with depth in 3D fluorescence microscopy

C. KERVRANN, D. LEGLAND & L. PARDINI
INRA – Unité de Biométrie et Intelligence Artificielle, Domaine de Vilvert, 78352 Jouy-en-Josas, France

Key words. 3D microscopy, fluorescence, image restoration, intensity loss, photobleaching, depth correction, confocal microscopy, robust estimation, regularization, computer vision.

Summary

Fluorescent signal intensities from confocal laser scanning microscopes (CLSM) suffer from several distortions inherent to the method. Namely, layers which lie deeper within the specimen are relatively dark due to absorption and scattering of both excitation and fluorescent light, photobleaching and/or other factors. Because of these effects, a quantitative analysis of images is not always possible without correction. Under certain assumptions, the decay of intensities can be estimated and used for a partial depth intensity correction. In this paper we propose an original robust incremental method for compensating the attenuation of intensity signals. Most previous correction methods are more or less empirical and based on fitting a decreasing parametric function to the section mean intensity curve computed by summing all pixel values in each section. The fitted curve is then used for the calculation of correction factors for each section and a new compensated sections series is computed. However, these methods do not perfectly correct the images. Hence, the algorithm we propose for the automatic correction of intensities relies on robust estimation, which automatically ignores pixels where measurements deviate from the decay model. It is based on techniques adopted from the computer vision literature for image motion estimation. The resulting algorithm is used to correct volumes acquired in CLSM. An implementation of such a restoration filter is discussed and examples of successful restorations are given.

1. Introduction

Loss of intensity is a well-recognized problem in both wide-field and confocal imaging, but there is no single method correction of 3D images that is applicable to all studies (Markham & Conchello, 2001). Indeed, there are many factors that contribute to intensity loss, and it is not always possible to define the contribution of all factors to this effect for each individual image and study (Rodenacker *et al.*, 2001). Consequently, various empirical methods have been used to correct images for the effects of the intensity loss before visualization and quantitative image analysis (e.g. Liljeborg *et al.*, 1995; Rodenacker *et al.*, 2001). In Fig. 1, the difficulty of the correction problem is exemplified from two biological images corresponding to sections taken at two different depths from a CLSM stack. We can see some geometrical features that have similar appearance in the two sections. However, because they were acquired at two different depths, features appear to be different in the two images; in this example, there are particularly dramatic differences in the intensity levels.

When a 3D fluorescence image (stack) is obtained with a CSLM, deeper layers in the specimen are imaged with lower photon intensity due to scattering and absorption of both excitation and fluorescence light and photobleaching (Centonze & Pawley, 1995; Tsien & Waggoner, 1995). This is sometimes accompanied by shading and some loss of detail. All these effects severely restrict a quantitative analysis of the images (Rigaut & Vassy, 1991). Indeed, a common way to extract objects for further measurement consists in applying a constant threshold in the digitized volume (Irinopoulo *et al.*, 1997; Rodenacker *et al.*, 1997). This threshold can no longer be constant throughout the volume because, due to light scattering and absorption, the deeper lying sections are weaker in intensity than the top most sections (Ortiz de Solorzano *et al.*, 1999; Rodenacker *et al.*, 2001). Prior to any extraction of objects a compensation for this light attenuation in lower lying parts of the specimen must be then applied. In fact, it has been shown in CLSM studies that the rate of photobleaching, which mainly contributes to intensity loss, varies along the depth direction or z-axis) (van Oostveldt *et al.*, 1998). The possibility of spatial heterogeneity

Correspondence to: Charles Kervrann. Tel.: (+33) 1 34 65 22 35; fax: (+33) 1 34 65 22 17; e-mail: ckervran@irisa.fr

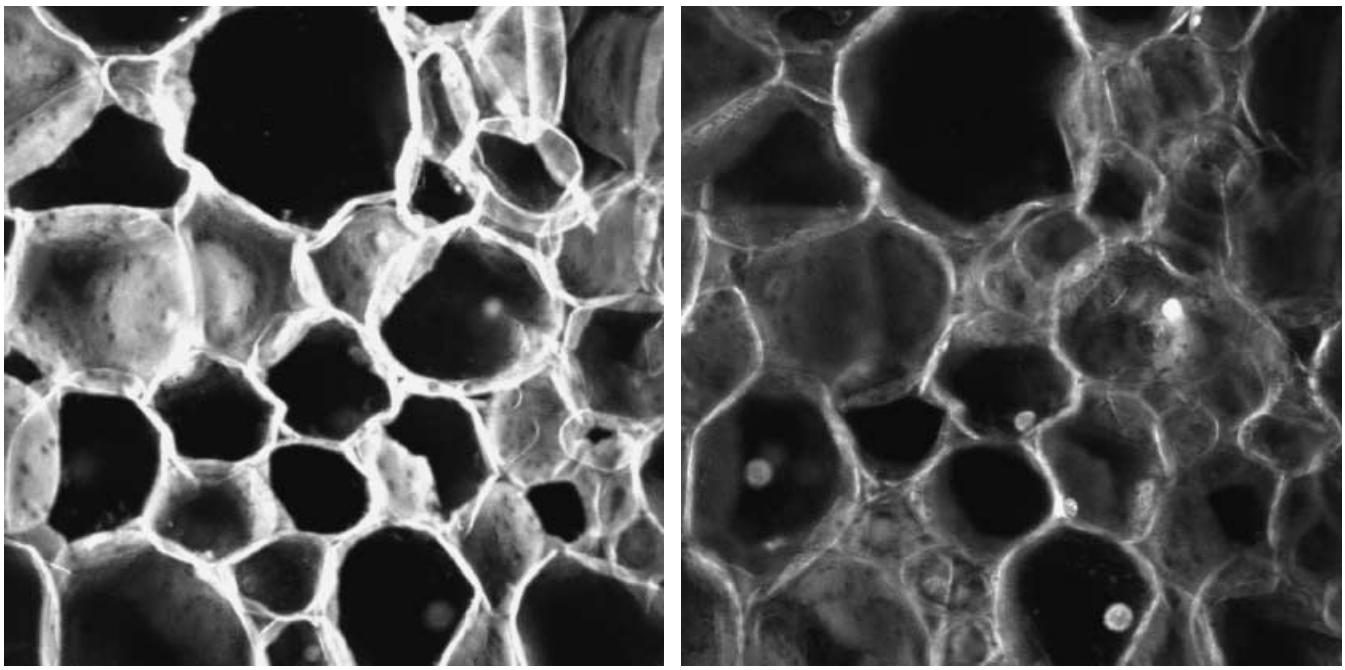

Fig. 1. Two sections of an original CLSM stack made of 40 sections. (a) Section 15; (b) Section 25.

appears to be largely ignored in correction studies, and most authors assume that the rate of photobleaching in a 3D image is spatially homogeneous and can be described by an exponential function of depth (e.g. Rigaut & Vassy, 1991), which has been shown to be adequate in many situations. However, it has been shown that, under certain well-defined conditions, bleaching of a thin, spatially uniform fluorescent test layer in both conventional and confocal microscopy is best described by a bi-exponential curve (Ghauharali *et al.*, 1998; Markham & Conchello, 2001).

There are several *ad-hoc* methods in the literature for the correction of sections (e.g. Rodenacker *et al.*, 2001). Because manual correction is a tedious, time-consuming and unreliable task and we wish to obtain a reliable distinction between background and objects of interest (Rigaut & Vassy, 1991), it is desirable to have automatic correction tools. Moreover, precise automatic correction is valuable not only in the example research study described above, but in many situations involving repeated CLSM acquisitions for the same subject. To address this problem, an iterative correction method based on an approximated inversion of the CLSM transfer function was proposed in Visser *et al.* (1991) and later improved by Roerdink & Bakker (1993) using the Fourier transform; a method based on the study of the stack 2-D histograms that can be formed for each consecutive pair of sections has been also applied to calculate the attenuation factor in Liljeborg *et al.* (1995). Here, the approach we have taken for image attenuation compensation is inspired by methods used for image motion estimation (Black & Rangarajan, 1996; Black & Anandan, 1996; Odobez & Bouthemy, 1995; Sawhney & Ayer, 1996; Negahdaripour, 1998; Germain *et al.*, 1999; Haussecker & Fleet, 2001) and image registration (Nestares & Heeger, 2000) in computer vision. Indeed, most image correction techniques rely on the assumption that both scattering and absorption are assumed to be governed by an exponential decay law with increased depth within the specimen (Rigaut & Vassy, 1991; Chen *et al.*, 1995; Ghauharali *et al.*, 1998; Ghauharali & Brakenhoff, 2000; Murray, 1998), a model already studied in Negahdaripour (1998) and Haussecker & Fleet (2001). So, we propose an algorithm for the automatic correction of CLSM images that relies on robust estimation (Huber, 1981) to compute the correction parameters: the resulting estimation procedure automatically ignores those pixels (outliers) where the decay model is violated. This compensation is important not only for the correct extraction of the objects by thresholding but, even more importantly, for the quantification of fluorophores, which is the primary goal of many applications.

The rest of the paper is organized as follows: in Section 2, we evaluate the accuracy of the exponential model and describe a numerical implementation of the robust estimation of the correction parameters. In Section 3, we present experimental results obtained by applying the algorithm to real 3D confocal images. Conclusions are drawn in the last part of the paper.

2. Methods

In this section, we evaluate the exponential decay law for modelling scattering and absorption, and photobleaching. We also describe a gradient-based approach used for estimating the related attenuation factors. In our context, a robust estimation method is used to estimate the correction parameters. This section ends with details regarding the implementation of the algorithm.

2.1. Assumptions

To estimate the intensity decay function, several basic model assumptions have to be considered (Rodenacker *et al.*, 2001): (*i*) homogeneity of medium with depth, (*ii*) independence of emission with depth, (*iii*) transparency of stained objects with depth, (*iv*) constant background noise intensity with depth and (*v*) sufficiently distributed emitting material with depth. However, some of these factors cannot be modelled theoretically. Assumptions are then necessary for simplification of the correction function estimation as well as for the correction itself. Assumptions (*i*), (*ii*) and (*v*) are critical for the estimation of the decay function. Generally, a homogeneous exponential model decay function gives an acceptable partial correction of depth influences (Rigaut & Vassy, 1991; Chen *et al.*, 1995; Ghauharali *et al.*, 1998; Ghauharali & Brakenhoff, 2000; Murray, 1998). In the following, we have also adopted this simple parametric modelling.

First, loss of intensity is assumed to be modelled by an exponential decay function:

$$\bar{I}_z = \bar{I}_0 e^{-kz} \tag{1}$$

where the subscript $z = 0, 1, \ldots, N_z$ is the section (or depth) index, $\bar{I}_z$ is the average intensity computed by summing all pixel values of section z, $\bar{I}_0$ is the average intensity of the bleachable component before bleaching and k is a constant that controls the rate of intensity loss (bleaching rate). In Eq. (1) we expressed the intensity loss only as a function of depth. This modelling is also possible for wide-field microscopes where optical sections are collected sequentially with identical exposure times. There are other factors, such as attenuation of fluorescent intensity due to tissue depth, that are also proportional to depth. Two more general forms of exponential functions are also allowed to describe the intensity decay with depth: a single exponential function plus a constant term (Murray, 1998) and the sum of two exponential functions (Ghauharali *et al.*, 1998; Markham & Conchello, 2001), i.e.

$$\bar{I}_z = Ae^{-k_A z} + Be^{-k_B z}, \tag{2}$$

have been proposed, where $z = 0, 1, \ldots, N_z$, $\bar{I}_z$ is the average intensity of section z, A and B are the coefficients for the two exponential terms, and k_A and k_B are the two exponential rate constants.

For solving Eq. (1), a straightforward search procedure was carried out by log-linear fitting of the curve (i.e. the value that gave the smallest residual sum of squared deviations of the data from a calculated single exponential decay curve) (Murray, 1998). Moreover, a non-linear weighted least-squares method is used to estimate the parameters of the bi-exponential model (see Eq. 2) for the the best fit to the section-intensity data curve in Markham & Conchello (2001). Finally, for correction, every pixel in section z is multiplied by a factor that is the ratio of the fitted value at the first section to the fitted value at section z. The estimated parameters are all constrained to be positive so that the exponential function neither increases nor becomes negative (Markham & Conchello, 2001).

In our approach to correct intensities loss, we made use of the fact that variations in the attenuation parameters with depth are relatively small. A robust gradient-based approach is then proposed to estimate the attenuation factors involved.

2.2. Gradient-based image correction

The intensity decreasing with depth can be approximated by an exponential decay model. From Eq. (1), the brightness function $I_z(x, y)$ has the following analytical form:

$$I_z(x, y) = I_0(x, y)\, e^{-kz}, \forall (x, y) \in G_z, \tag{3}$$

where $\mathbf{x} = (x, y)$ denotes the spatial coordinates of the 2D discrete image domain G_z (or section z) of N pixels, and $I_z(\mathbf{x})$ is the grey-level value at location $\mathbf{x}$ in section z. The partial derivative along the z-axis of both sides of Eq. (3) then yields the following brightness constraint equation:

$$\frac{dI_z(\mathbf{x})}{dz} = -kI_0(\mathbf{x})e^{-kz} = -kI_z(\mathbf{x}). \tag{4}$$

This differential equation states that the rate of change at any depth is proportional to the current value. Hence, our brightness constraint equation is linear in the decay parameter k. In this paper, we investigate new methods for the computation of correction factors based on the following extended linear model:

$$\Delta I_z(\mathbf{x}) \approx -kI_z(\mathbf{x}) - m \tag{5}$$

where $\Delta I_z(\mathbf{x}) = I_z(\mathbf{x}) - I_{z+1}(\mathbf{x})$ is the numerical approximation of the partial derivative $\frac{dI_z(x, y)}{dz}$ along the z-axis computed for two immediately consecutive sections. This model allows linear transformation of the brightness of an image point, from one section to the next, described by a rate k and an offset m. It incorporates effects from any event that changes the image brightness of a point through a linear transformation. This modelling permits changes in contrast and mean intensity but is valid only if stacks show a small decrease of the global intensity. Previous methods are more limited because the parameters

of the decay models are estimated based on the assumption that the fluorophore density is constant along the depth, which is not the case for most types of biological specimen as the intensity variation is also a function of the geometry. Nevertheless, the fluorophore density is probably more constant between two consecutive sections, which is the main assumption of the current method; this does not mean the parameters are constant along the depth.

Now, let $\theta = (k, m)$ denote the vector of unknown parameters we wish to estimate. If we consider all the pixels based on physical considerations, we obtain the following over-determined linear system from Eq. (5):

$$\begin{pmatrix} \Delta I_z(\mathbf{x}_0) \\ \Delta I_z(\mathbf{x}_1) \\ \vdots \\ \Delta I_z(\mathbf{x}_N) \end{pmatrix} = \begin{pmatrix} -I_z(\mathbf{x}_0) & -1 \\ -I_z(\mathbf{x}_1) & -1 \\ \vdots & \vdots \\ -I_z(\mathbf{x}_N) & -1 \end{pmatrix} \theta^T \tag{6}$$

where the subscript i indexes all the pixels of the image-section z, N is the number of pixels of the section z and the superscript T denotes the transpose operator. This over-determined system can be solved using conventional least-squares methods: the least-squares solution of the system minimizes the sum over all pixels of the squared residual errors, defined as $r_i^2 = (\mathbf{u}(\mathbf{x}_i; \theta) - \Delta I_z(\mathbf{x}_i))^2$ where $\mathbf{u}(\mathbf{x}_i; \theta) = -kI_z(\mathbf{x}_i) - m$. However, the least-squares solution is very sensitive to isolated points having high residual errors. In principle, one very poor pixel $\mathbf{x}_i$ with a very large residual r_i can corrupt the solution. Alternative error functions then have to be used. Robust regression techniques are generally adequate to avoid the influence of pixels that violate the intensity conservation assumption due to the different acquisition protocols. The resulting systems of equations can be solved using weighted least squares with a small number of parameters that simultaneously characterize the attenuation of all pixels.

2.3. Robust statistics

Robust statistical estimation techniques have been designed to find the parameter vector which best fits a model to the observations when some data contain gross errors or behave like *outliers*. For mathematical details the reader is referred to Huber (1981), Hampel *et al.* (1986) and Rousseeuw & Leroy (1987). Many robust statistical techniques have been applied to standard problems in computer vision (Meer *et al.*, 1991) such as local image smoothing (Black *et al.*, 1998), image reconstruction (Black & Rangarajan, 1996), image registration (Nestares & Heeger, 2000), optical flow estimation (Black & Rangarajan, 1996; Black & Anandan, 1996; Odobez & Bouthemy, 1995; Sawhney & Ayer, 1996; Germain *et al.*, 1999).

Robust estimators. As identified by Hampel *et al.* (1986), the main goals of robust statistics are: (*i*) to describe the structure of the bulk of the data; (*ii*) to identify deviating data points (outliers) or deviating substructures for further treatment, if desired. To state the issue more concretely, robust statistics address the problem of finding the parameters vector $\theta = (\theta_1, \ldots, \theta_p)$ that provide the best fit of a model, i.e. $\mathbf{u}(\mathbf{x}_i; \theta)$, to a set of N data measurements $\mathbf{d} = \{d_0, \ldots, d_N\}$ which may be corrupted by gross errors (in our application, $p = 2$, $\theta_1 = k$, $\theta_2 = m$, and $d_i = \Delta I_z(\mathbf{x}_i)$). This problem is then equivalent to finding the parameter vector θ that minimizes the sum of a function of the residual errors $r_i = (d_i - \mathbf{u}(\mathbf{x}_i; \theta))$. In the robust statistics framework, this sum does not grow indefinitely (in contrast to the squared function used by least-squares), but rather saturates for large residual errors. This yields

$$\hat{\theta} = \arg\min_{\theta} \sum_i \rho(d_i - \mathbf{u}(\mathbf{x}_i; \theta), \sigma_\rho), \quad i = 1, \ldots, N \tag{7}$$

where the subscript i denotes the index of the ith image pixel, σ_ρ is a scale parameter and ρ is our error norm. The ρ-function is also called an M-estimator because this minimization corresponds to the maximum-likelihood estimation, if ρ is interpreted as the opposite of the conditional log-likelihood of the observations $\mathbf{d}$. Note that when the errors in the measurement are normally distributed, the optimal ρ-function has a quadratic form:

$$\rho(d_i - \mathbf{u}(\mathbf{x}_i; \theta), \sigma_\rho) = \frac{(d_i - \mathbf{u}(\mathbf{x}_i; \theta))^2}{2\sigma_\rho^2} \tag{8}$$

which gives rise to the standard *least-squares* estimation problem. The problem with the *least-squares* solution is that the outlying points are assigned a high weight, which is not desirable when data contain outliers. To eliminate the contribution of these outliers, a hard redescending ρ-norm should be more appropriate. This results in different robust estimators and the robustness of a particular estimator refers to its insensitivity to outliers, or deviations, from the assumed statistical model.

Furthermore, to analyse the behaviour of a ρ-function, we take the approach of Hampel *et al.* (1986) based on influence functions. The influence function characterizes the bias that a particular measurement has on the solution and is proportional to the derivative ψ, of the ρ-function. Consider, for example, the quadratic ρ-function (Fig. 2a,b)

$$\rho(r) = r^2, \quad \psi(r) = 2r. \tag{9}$$

For least-squares estimation, the influence of outliers increases linearly and without bound. Now consider the following Geman & McClure (1987) estimator:

$$\rho(r, \sigma_\rho) = \frac{r^2}{\sigma_\rho^2 + r^2}, \quad \psi(r, \sigma_\rho) = \frac{2r\sigma_\rho^2}{(\sigma_\rho^2 + r^2)^2} \tag{10}$$

plotted along with its ψ-function in Fig. 2(c,d). Examination of this ψ-function reveals that when the absolute value of a residual increases beyond a threshold characterized by σ_ρ, its influence decreases.

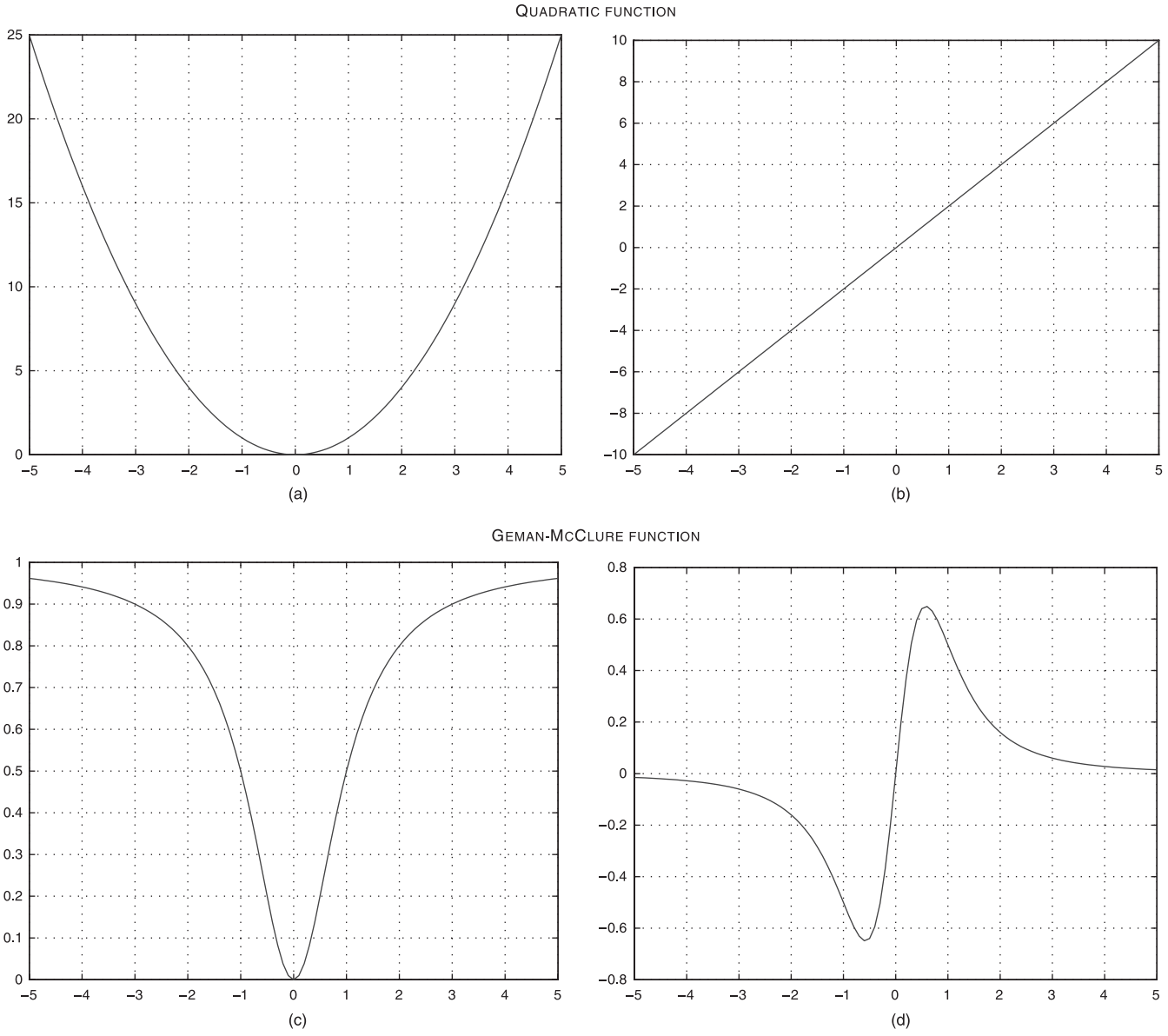

Fig. 2. Common ρ-functions and their derivatives ψ: (a) $\rho(r) = r^2$; (b) $\psi(r) = 2r$; (c) $\rho(r, \sigma_\rho) = \frac{r^2}{r^2 + \sigma_\rho^2}$; (d) $\psi(r, \sigma_\rho) = \frac{2r\sigma_\rho^2}{(r^2 + \sigma_\rho^2)^2}$.

Iteratively reweighted least squares. Given a robust estimator, the problem is now to find the parameter vector θ that minimizes a robust cost function that evaluates the error made on the model. This can be accomplished by taking the objective function written in terms of robust ρ-functions (see Eq. 7) and derive a new objective function to minimize, such that:

$$\sum_i \rho(r_i, \sigma_\rho) = \sum_i \frac{1}{2} w_i r_i^2 \quad \text{with} \quad r_i = d_i - \mathbf{u}(\mathbf{x}_i; \theta), \quad (11)$$

where w_i are appropriate weights. This so-called *iteratively reweighted least squares* (IRLS) method then converts the M-estimation problem into an equivalent *weighted least-squares* problem. A necessary condition for minimization is that the derivatives of the error measure with respect to each component θ_j of the parameters vector $\theta = (\theta_1, \ldots, \theta_p)$ are null. So we get

$$\sum_i \psi(r_i) \frac{\partial r_i}{\partial \theta_j} = \sum_i w_i r_i \frac{\partial r_i}{\partial \theta_j} = 0, \quad j = 1, \ldots, p. \quad (12)$$

The weights w_i at each data point $\mathbf{x}_i$ are therefore given by

$$w_i = \frac{\psi(r_i)}{r_i}. \quad (13)$$

The following estimation algorithm is then proposed. The first IRLS step consists in obtaining a first estimate of θ using $w_i = 1$, $i = 1, \ldots, N$; in that case, all data are regarded as inliers. Because the model $\mathbf{u}(\mathbf{x}_i; \theta)$ is linear with respect to the parameter θ, this can be achieved using least squares minimization. Then, weights are evaluated using Eq. (13), and a new estimate of θ is computed using weighted least squares. The process is repeated until convergence and the weights are updated at each iteration such that those points displaying greater residual errors are given less weight in the next iteration. From a practical point of view, the minimization is led alternately with respect to θ on the one hand, and with respect to the w_is on the other hand:

- the w_is being 'frozen', the minimization in θ becomes:

$$\hat{\theta} = \arg\min_{\theta} \sum_i \frac{1}{2} w_i r_i^2. \tag{14}$$

This weighted least squares problem is equivalent to the resolution of a linear system.

- θ being 'frozen', the minimization with respect to weights yields

$$w_i = \frac{\psi(r_i)}{r_i}, \quad i = 1, \ldots, N. \tag{15}$$

The two steps are repeated until convergence or when a maximum number of iterations is reached (Odobez & Bouthemy, 1995). Note that when the residual $|r_i|$ becomes larger, the corresponding optimal weight w_i becomes smaller and smaller, providing the robustness of the estimator. One problem with the robust estimators is that the resulting function to be minimized is non-convex, and thus there is no guarantee of convergence to a global minimum. Therefore, it is necessary to start with an initial condition close to the absolute minimum. The accurate estimates obtained in our experimental results confirm that the algorithm is almost always converging to the global minimum, or at least to a nearby local minimum if we choose $w_i = 1$, $i = 1, \ldots, N$, as initial conditions.

Finally, there are numerous ρ-functions that have been used in the computer vision literature, each with different motivations and strengths, but their common property is their ability to reduce the effect of outliers. In the remainder of this paper, we consider the Geman–McClure function, plotted along with its influence function in Fig. 2c,d, which gives nonzero descending weights. This function has a differentiable ψ-function which provides a gradual transition between inliers and outliers.

'Robust' scale. Also, the ρ-function have scale parameters which allow the shape of the function to be changed. We use tools from 'robust statistics' to estimate automatically the scale parameter σ_ρ of the data from residuals (Sawhney & Ayer, 1996; Black *et al.*, 1998). The deviation σ_e of residuals can in fact be related to the constant σ_ρ appearing in the ρ-function. Given contaminated data from a zero-mean Gaussian distribution, a robust estimate of σ_e is related to the residuals through

$$\begin{aligned} \sigma_e &= 1.4826 \times \mathrm{MAD}(r_i) \\ \sigma_e &= 1.4826 \times \mathrm{median}_i(|\, r_i - \mathrm{median}_j(r_j)\,|) \end{aligned} \tag{16}$$

where 'MAD' denotes the median of absolute deviation taken over all the pixels, $i = 1, \ldots, N$, and the constant derived from the fact that the MAD of zero-mean normal distribution with unit variance is $0.6745 = 1/1.4826$. The median-based estimate has an excellent resistance to outliers; it can tolerate almost 50% of them, and can be efficiently computed with a linear time median-finding algorithm. To estimate σ_ρ, one possibility is to choose values for the scale parameters σ_ρ so they begin rejecting outliers at the value σ_e. The point where the influence of outliers first begins to decrease as the magnitude of the residuals increases for zero occurs when the derivative of the ψ-function is zero. For the Geman–McClure norm it occurs at $\sigma_e = \sigma_\rho/\sqrt{3}$ and residuals $|\, r_i \,|$ greater than σ_e are considered as outliers. Furthermore, a binary mask of regions of outliers can be also generated. Note that this binarization is only a post-processing step for display purposes, whereas the computation of attenuation parameters uses the continuous weights derived from the ρ-function.

2.4. Regularization

This step has been implemented to complete and stabilize the estimation of the parameters vector $\theta = (k, m)$. We make the assumption that parameters are slowly evolving with regard to the depth sampling frequency. The estimates k and m usually must present smooth variations from one section to the next. Accordingly, a regularization can be implemented by adding a smoothness constraint on the set $\{\theta_1, \ldots, \theta_{N_z}\}$ where N_z is the total number of sections in the stack.

The maximum *a posteriori* (MAP) estimation is a popular Bayesian formulation of regularization techniques according to the general scheme of balancing between trust to data and fidelity to priors (i.e. constraints). It consists in finding an estimator of θ that maximizes the posterior probability distribution of θ given the data $\mathbf{d} = \{d_1, \ldots, d_N\}$:

$$\hat{\theta} = \arg\max_{\theta} P(\theta \mid \mathbf{d}) \tag{17}$$

$$= \arg\max_{\theta} P(\mathbf{d} \mid \theta)\, P(\theta). \tag{18}$$

The likelihood $P(\mathbf{d} \mid \theta)$ measures the distortion between the observation data and the model and $P(\theta)$ is the *a priori* probability distribution of θ which gathers the priors.

With a Bayesian approach, the M-estimation described in Section 2.3 is actually equivalent to the maximum likelihood estimation:

$$\hat{\theta} = \arg\max_{\theta} P(\mathbf{d} \mid \theta) \tag{19}$$

$$= \arg\max_{\theta} \left\{ \prod_i \exp\left[-\frac{1}{2} \rho(r_i, \sigma_\rho) \right] \right\} \tag{20}$$

$$= \arg\min_{\theta} \left\{ \sum_i \rho(r_i, \sigma_\rho) \right\}. \tag{21}$$

We can now introduce the *a priori* smoothness constraint on θ in $P(\theta)$. A widely used formalism for regularization consists in using the following *a priori* term:

$$P(\theta) \quad \propto \quad \exp - [(\theta - \theta')^T \Lambda (\theta - \theta')] \tag{22}$$

$$\propto \quad \exp - \left[\frac{\| k - k' \|^2}{2\sigma_k^2} + \frac{\| m - m' \|^2}{2\sigma_m^2} \right] \tag{23}$$

where θ' is the estimate of θ in the immediately preceding section, σ_k^2 and σ_m^2 are the variances associated with the variations of parameters k and m between two consecutive sections and Λ is a 2×2 diagonal matrix: $\Lambda = \mathrm{diag}\,(\sigma_k^2,\ \sigma_m^2)$. The corresponding function is quadratic, which means that the emergence of discontinuities between two consecutive estimates of θ is severely punished.

As a primary conclusion, we may write the MAP estimator of θ as:

$$\hat{\theta} = \arg\max_{\theta} P(\mathbf{d} \mid \theta) P(\theta) \tag{24}$$

$$= \arg\max_{\theta} \exp - \left[\sum_i \frac{1}{2} \rho(r_i, \sigma_\rho) \right] \cdot \exp - \left[\frac{\| k - k' \|^2}{2\sigma_k^2} + \frac{\| m - m' \|^2}{2\sigma_m^2} \right] \tag{25}$$

which is equivalent to the minimization of the following regularized energy:

$$\sum_i \rho(r_i, \sigma_\rho) + \frac{\| k - k' \|^2}{\sigma_k^2} + \frac{\| m - m' \|^2}{\sigma_m^2}. \tag{26}$$

For the IRLS implementation, we have then to solve (see Eq. 14):

$$\hat{\theta} = \arg\min_{\theta} \sum_i \frac{1}{2} w_i r_i^2 + \frac{\| k - k' \|^2}{\sigma_k^2} + \frac{\| m - m' \|^2}{\sigma_m^2}. \tag{27}$$

Here, the first quadratic term means that the norm of the MAP estimate deviation from data should be as small as possible, and the other terms enforce smoothness. The variances σ_k^2 and σ_m^2 are used to set a balance between the likelihood function – quantifying the faithfulness to the data – and an *a priori* term with regards to estimator behaviour as we have seen before. Great effort has been made to set these variances from data but usually it leads to non-tractable algorithms. Therefore, σ_k^2 and σ_m^2 are chosen on an empirical basis.

2.5. Implementation details

The estimation algorithm. The *weighted least squares* problem (Eq. 27) is equivalent to the resolution of some linear system. This yields:

$$\begin{pmatrix} \hat{k} \\ \\ \hat{m} \end{pmatrix} = \begin{pmatrix} \sum_{i=1}^{N} w_i I_z(\mathbf{x}_i)^2 + \sigma_k^{-2} & \sum_{i=1}^{N} w_i^{1/2} I_z(\mathbf{x}_i) \\ \sum_{i=1}^{N} w_i^{1/2} I_z(\mathbf{x}_i) & N + \sigma_m^{-2} \end{pmatrix}^{-1} \begin{pmatrix} k'\sigma_k^{-2} - \sum_{i=1}^{N} w_i I_z(\mathbf{x}_i) \Delta I_z(\mathbf{x}_i) \\ m'\sigma_m^{-2} - \sum_{i=1}^{N} w_i^{1/2} \Delta I_z(\mathbf{x}_i) \end{pmatrix} \tag{28}$$

where k' and m' are the estimates of k and m obtained for the immediately preceding section of the stack numbered from 0 to N_z. This computation (Eq. 28) is performed at each iteration of the IRLS algorithm, summarized as follows:

begin
  initialization: $w_i = 1, i = 1, \ldots, N$
  do
    update k and m according to Eq. (28)
    update $w_i = \dfrac{\psi(r_i)}{r_i}, i = 1, \ldots, N$
  until convergence
end

This algorithm is running for each section while k' and m' are updated. Note the two updating steps are repeated until convergence (i.e. there is no change in the parameters between two successive iterations) or when a maximum number of iterations is reached.

Image warping. We have proposed an IRLS algorithm to estimate attenuation parameters $\theta = (k, m)$ robustly between two consecutive sections. Now, we need to compensate this attenuation for each section of the stack. To restore sections, a simple idea is to take one section as reference and then to compensate all the other sections with respect to the chosen section. Choosing the reference section is performed manually: it corresponds naturally to one section among the sections located at the top of the stack (for instance at depth 0), if the specimen is scanned from top to bottom. The reference section is not changed by the restoration process and all the successive sections, from top to bottom, are restored with respect to the reference section.

Formally, we have (see Eq. 5):

$$I_z(\mathbf{x}) - I_{z+1}(\mathbf{x}) \approx -k_z I_z(\mathbf{x}) - m_z \tag{29}$$

where k_z and m_z denote the attenuation parameters at depth z. An approximation of $I_z(\mathbf{x})$ based on $I_{z+1}(\mathbf{x})$ is then given by:

$$I_z(\mathbf{x}) \approx \frac{I_{z+1}(\mathbf{x}) - m_z}{1 + k_z}. \tag{30}$$

Similarly, an approximation of $I_{z+1}(\mathbf{x})$ based on $I_{z+2}(\mathbf{x})$ is given by:

$$I_{z+1}(\mathbf{x}) \approx \frac{I_{z+2}(\mathbf{x}) - m_{z+1}}{1 + k_{z+1}} \tag{31}$$

and therefore

$$I_z(\mathbf{x}) \approx \frac{\dfrac{I_{z+2}(\mathbf{x}) - m_{z+1}}{1 + k_{z+1}} - m_z}{1 + k_z}. \tag{32}$$

By summing all estimation results, a restored image $I^r_{z+n}(\mathbf{x})$ computed from an original section $I_{z+n}(\mathbf{x})$, with reference to an initial section $I_z(\mathbf{x})$ chosen by the user, is obtained as:

$$I^r_{z+n}(\mathbf{x}) = g_{z,z+1} \circ g_{z+1,z+2} \circ \cdots \circ g_{z+n-1,z+n}(I_{z+n}(\mathbf{x})) \tag{33}$$

if we define $g_{z+n,z+n+1}(I.(\mathbf{x}))$ as:

$$g_{z+n,z+n+1}(I.(\mathbf{x})) = \frac{I.(\mathbf{x}) - m_{z+n}}{1 + k_{z+n}}. \tag{34}$$

Given an input section $I_{z+n}(\mathbf{x})$ at depth $z + n$ and n successive pairs of estimates $\{k_j, m_j\}_{j=z}^{j=z+n}$, the restored image is warped backwards with reference to the section z.

3. Experimental results

Before starting the automatic correction procedure it is necessary to provide a reference section as a starting point. This was performed manually and the remaining steps of the algorithm, implemented in C++ language, are fully automatic, taking 1–3 min running on a workstation equipped with an UltraSPARC-II 296-MHz processor and 1.7 Gb RAM. Unless specified, the values of the parameters used in all the experiments were the same as those used in previous sections. Priors tend to stabilize the algorithm so that it seeks a solution in the vicinity of those found in the previous depth samples. All the restored stacks were produced using the same set of parameters; in our experiments, $\sigma_m^2 = (10^{-2})^2$ and $\sigma_k^2 = (5.10^{-3})^2$ show better performance in estimating attenuation parameters.

Confocal images were acquired using a Zeiss LS 410 confocal microscope 410 equipped with two lasers (argon and UV lasers). The images were coded in 256 levels of grey. Conditions of acquisition were kept according to Pawley's (1990) recommendations for confocal microscopic analysis. The microscope acts as an 'optical microtome' allowing the sectioning of fluorescent-labelled cells sequentially and storage of each optical section digitally. In the first study, nuclear DNA of rat colonic cells along crypts was stained with Hoechst 33258 or propidium iodide (with sample pretreated by RNase I). The optical section thickness, and therefore the z-axis resolution, is a function of the numerical aperture of the lens and the aperture size of the adjustable confocal pinhole. In this study, the pinhole was set to eight arbitrary disk units for all fluorescent probes; it provides an x–y resolution of 160–180 nm and a z-sectioning space of 1 μm (according to the 730-nm maximal depth resolution described for fluorescent CSLM). Preparations were observed under a ×40 water immersion objective with a 1.2 numerical aperture and captured in a frame of 512 × 512 pixels (zoom factor of 1) with a 72-dot/inch resolution and four scans per image (scan time: 1 s). Stacks of images (x–y sections, 512^2 pixels) were collected with 80 images (by L. Pardini (INRA-Unité de Biométrie et Intelligence Artificielle, Jouy-en-Josas, France) and B. Kaeffer (INRA-UFDNH, Nantes, France)). The images were stored in TIF format and transferred to a UNIX work-station for analysis. We choose arbitrarily the section # 20 as the reference section (Fig. 3a). Hence, sections from 1 to 20 are unchanged in the restored stack. The restored images are obtained using the procedure described previously (see Section 2.5). In Fig. 3, we show the raw images (numbered from top to bottom) when there is loss of intensity but no correction for them. Figure 4 shows the results with the German–McClure ρ-function after 20 iterations. The value σ_e was automatically estimated and the values of σ_ρ were defined with respect to σ_e as: $\sigma_e = \sigma_\rho/\sqrt{3}$. The proposed approach detects spatial positions (pixels) when the exponential model is violated (i.e. $|r_i| > \sigma_e$). These violations (or outliers) appear as dark regions in Fig. 5 and inliers as white regions. Here, outliers correspond to non-stained regions and noise. Note that fluorescence values lower than 10 are not taken into account in this estimation procedure because these values are assumed to correspond to noise and background. Plots of the two parameters k and m with respect to the section index z are shown in Fig. 6. The parameters are not constant along the depth as expected but regularized. The section mean intensity curves when there is no correction (dashed line) and when correction for intensity loss is applied (solid line) are also shown in Fig. 7(a). If the sections contents (i.e geometric features) are homogeneous with respect to the section index, the restored mean intensity curve is ideally horizontal. Finally, the average contrast (noted C_z at depth z) curves, computed from the absolute difference between two successive sections as $C_z = \frac{1}{N}\sum_{i=1}^{N} |I_z(\mathbf{x}_i) - I_{z+1}(\mathbf{x}_i)|$ where N is the number of pixels per section, are shown in Fig. 7(b). Unlike the original images stack, the results indicate the restored stack does not exhibit a decrease in contrast with depth and quantitative information can be extracted.

In the second study, stacks of images were collected with 40 sections per stack showing tomato membranes (image

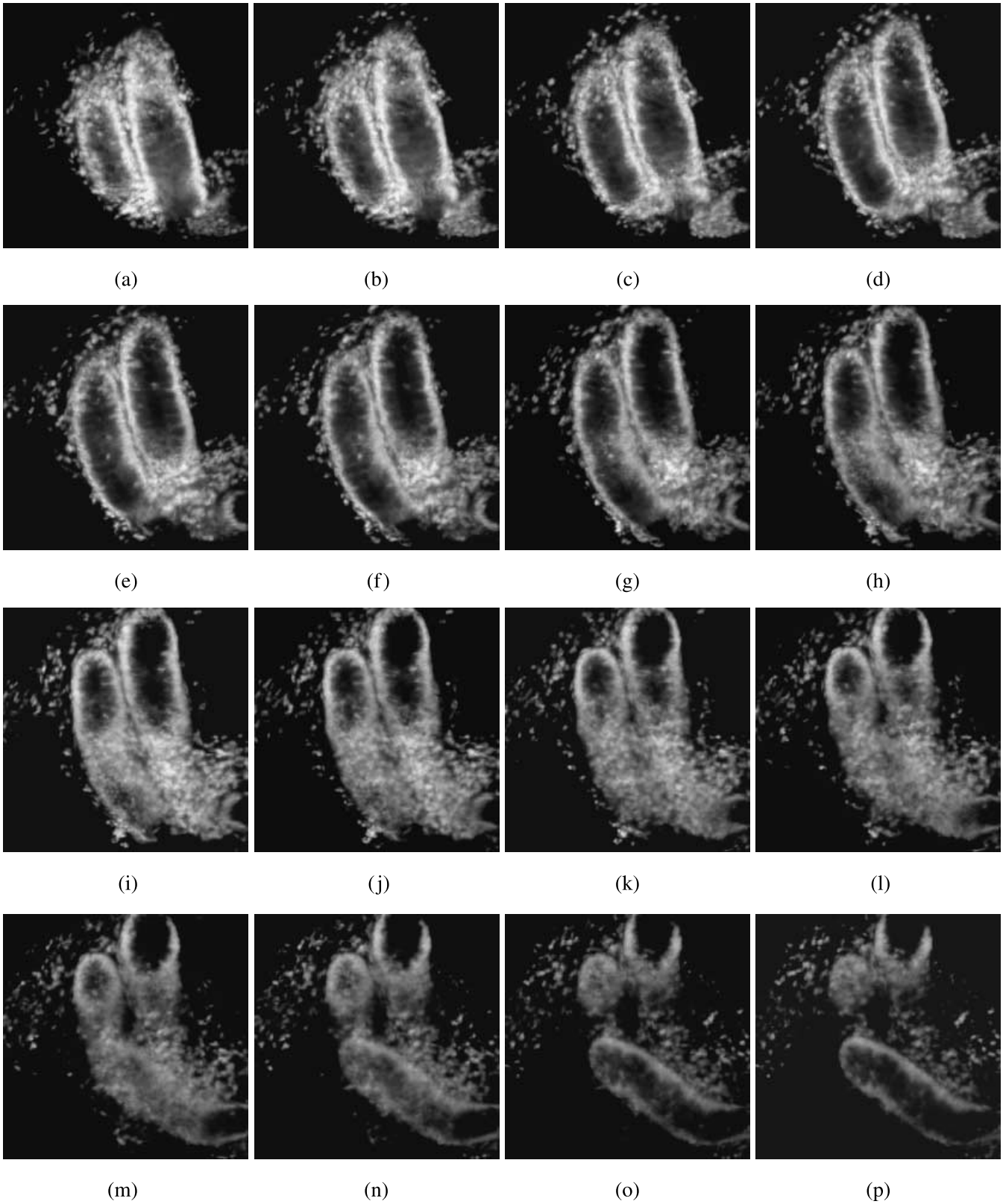

Fig. 3. Reference section # 20 and some sections from an original CLSM stack of 80 sections: (a) Section # 20, (b) Section # 24, (c) Section # 28, (d) Section # 32, (e) Section # 36, (f) Section # 40, (g) Section # 44, (h) Section # 48, (i) Section # 52, (j) Section # 56, (k) Section # 60, (l) Section # 64, (m) Section # 68, (n) Section # 72, (o) Section # 76, (p) Section # 80.

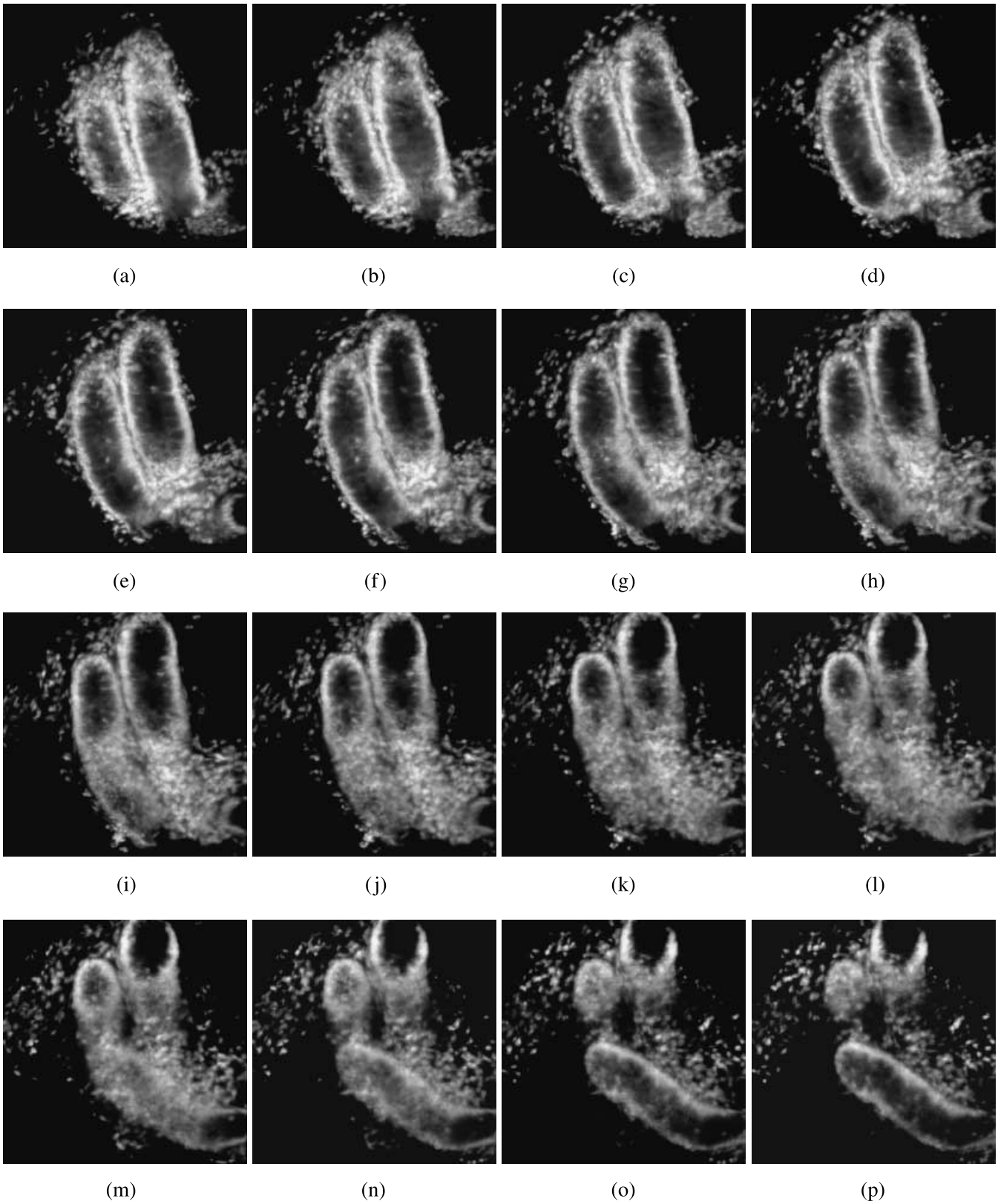

Fig. 4. Some sections from a restored CLSM stack of 80 sections: (a) Section # 20, (b) Section # 24, (c) Section # 28, (d) Section # 32, (e) Section # 36, (f) Section # 40, (g) Section # 44, (h) Section # 48, (i) Section # 52, (j) Section # 56, (k) Section # 60, (l) Section # 64, (m) Section # 68, (n) Section # 72, (o) Section # 76, (p) Section # 80.

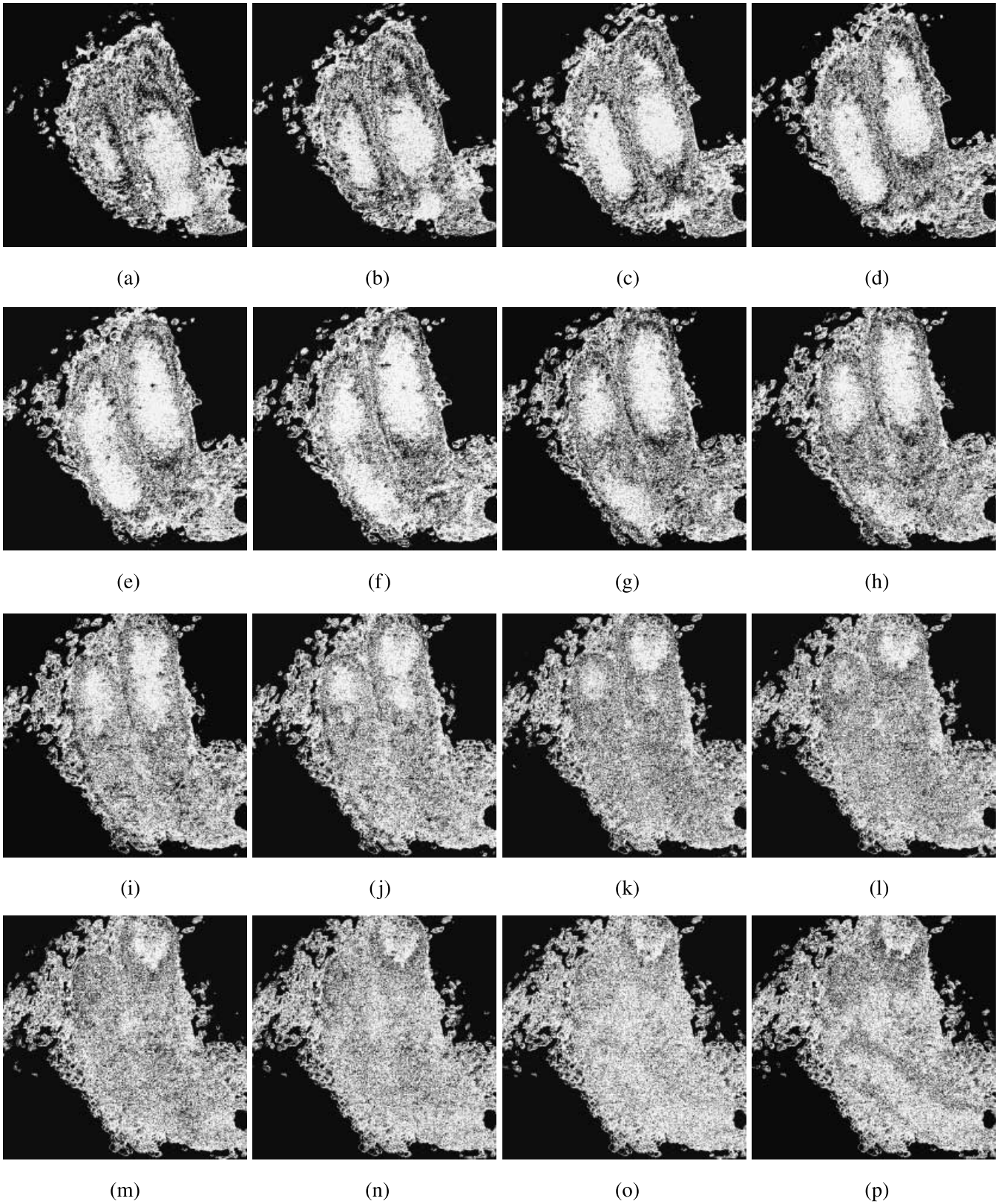

Fig. 5. Detection of outliers (black pixels) for some sections from a restored CLSM stack of 80 sections: (a) Section # 20, (b) Section # 24, (c) Section # 28, (d) Section # 32, (e) Section # 36, (f) Section # 40, (g) Section # 44, (h) Section # 48, (i) Section # 52, (j) Section # 56, (k) Section # 60, (l) Section # 64, (m) Section # 68, (n) Section # 72, (o) Section # 76, (p) Section # 80.

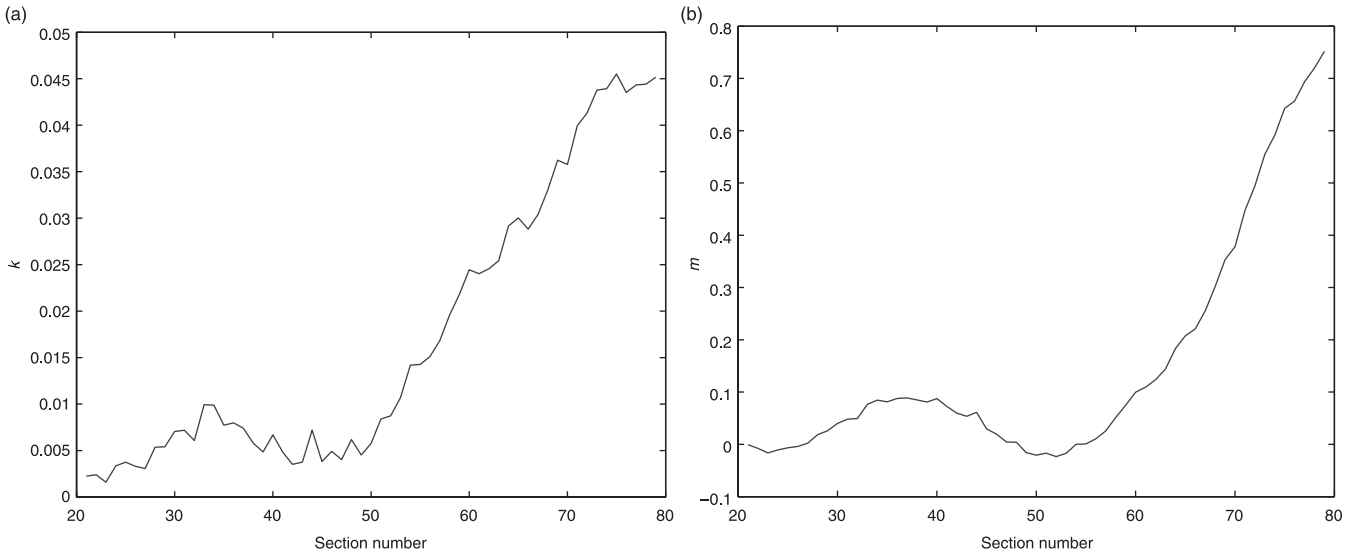

Fig. 6. Plots of attenuation parameters k and m against section number: (a) k against section number, (b) m against section number.

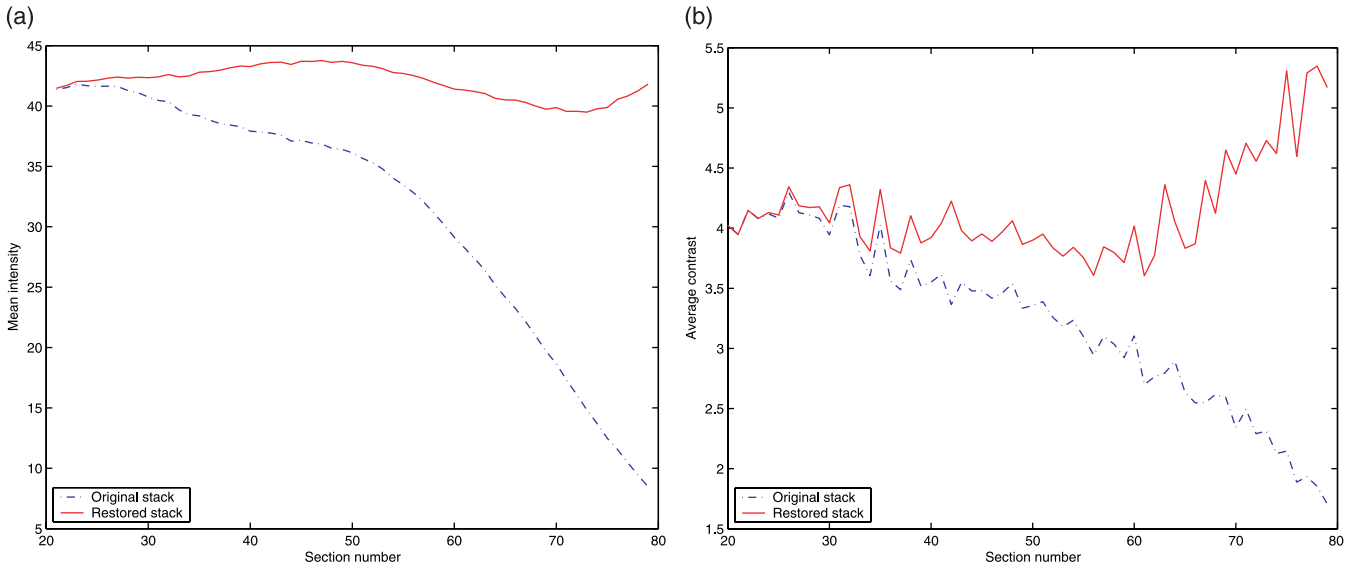

Fig. 7. Plots of the mean intensity and average contrast curves of the original and restored stacks: (a) mean intensity curves, (b) average contrast curves.

courtesy of M. F. Devaux, INRA-URPOI, Nantes, France, 2003) (Figs 8 and 9). The 200–250-μm tissue sections were stained with calcofluor 0.01%. The specimens were digitized using a ×10 air immersion objective with a numerical aperture of 0.5, giving a depth discrimination of about 5.0 μm. The z-step between each section was 5.0 μm. The sections were 512×512 pixels with a pixel size of 2.5×2.5 μm. The pinhole was set to seven arbitrary disk units for all fluorescent probes. The excitation wavelength was 364 nm and the light emitted over 397 nm was collected using a long-pass filter. Figure 8(a) shows the reference section # 12 arbitrarily chosen in the stack. Section # 39 of the stack is also shown in Fig. 8(b) for visualization purposes. A subset of images from the stack (numbered from top to bottom) when there is loss of intensity are shown in Fig. 9. Figure 10 shows the restoration results after 20 iterations of the IRLS algorithm (see Section 2.5). The image contrast is approximatively the same for all the restored sections, as expected. Parameters of the algorithm are the same as

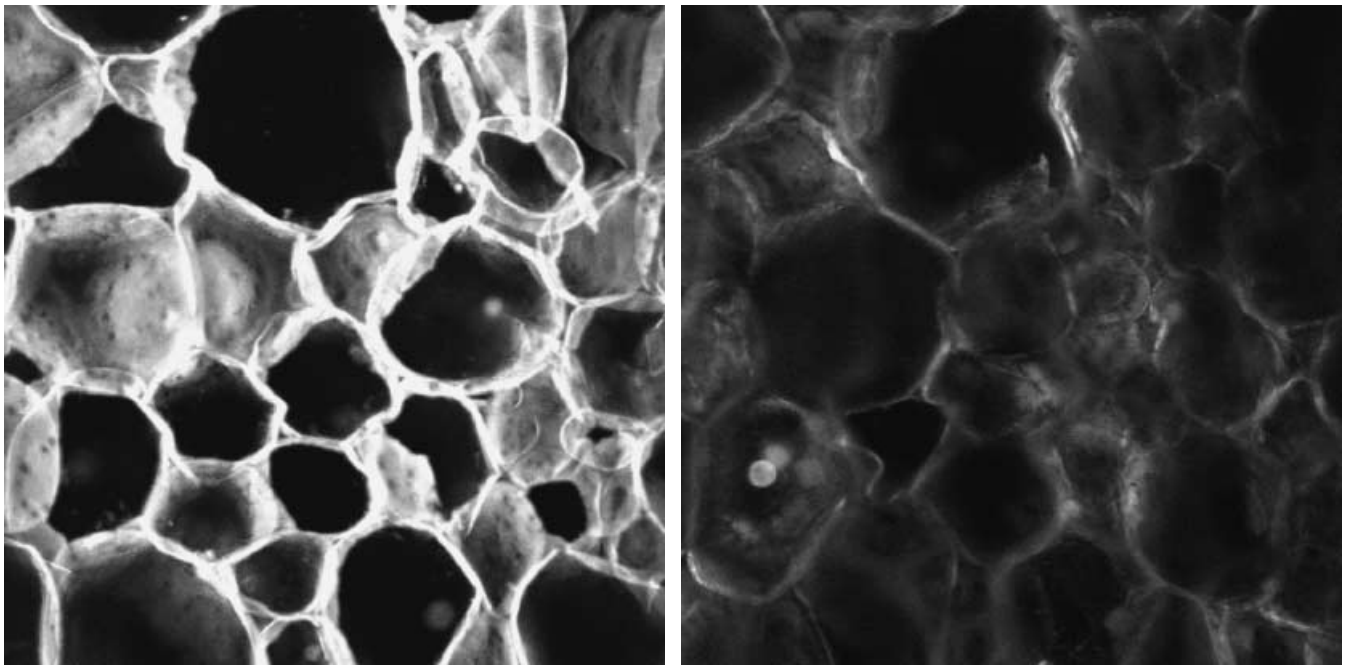

(a) (b)

Fig. 8. Reference section # 12 (a) and section # 39 (b) extracted from of the original stack.

those used in the previous experimental study and Sections 1 to 12 are unchanged in the restored stack. Additionally, the outliers are thresholded (black pixels) and displayed in Fig. 11. The evolution of attenuation parameters with respect to the section index z is shown in Fig. 12. The section mean intensity curves against section number when there is no correction (dashed line) and when correction for intensity loss is applied (solid line) are shown in Fig. 8(b). Finally, the average contrast curves of the original and restored stacks are shown in Fig. 13(b). As previously, the average contrast of the restored stack clearly does not decrease with depth in this study.

4. Discussion and conclusion

The aim of this study was to compensate loss of intensity in 3D fluorescence microscopy. We have presented a method to cope with loss of intensity due to photobleaching, attenuation of fluorescence in tissue depth or other factors. As we have shown, the distortions in restored intensity levels can be extreme and can cause large errors in the interpretation of restored images, especially if quantification is required. A simple and unsupervised correction method has been proposed for 3D fluorescence microscopy by using an exponential form to fit the data. In the compensation method used here, the absorption is not assumed to be constant throughout each section, i.e. the compensation factors are not constant but estimated for each section. This function is adaptively estimated using a gradient-based approach, robust statistics and regularization, without manual setting of any underlying optical attenuation constants. We only impose the attenuation coefficients (k, m) do not abruptly change between two successive sections and the thickness between two consecutive sections is not too large. In that sense, the method is limited for high-NA imaging. However, in practice we just need to assume the image contents are not too different between two consecutive sections whatever the z-resolution may be. Our compensation method contributes also to the accuracy of the quantification of fluorophores in 3D fluorescence microscopy; the experimental results clearly indicate the restored stacks do not exhibit a decrease in contrast with depth and pixels that violate the model may be isolated for further processing if desired.

Acknowledgements

We thank B. Kaeffer (INRA-UFDNH (Unité des Fonctions Digestives et Nutrition Humaine), Nantes, France) and M. F. Devaux (INRA-URPOI (Unité Recherche sur les Polysaccharides, leurs Organisations et leurs Interactions), Nantes, France) for the biological images used in the paper and for bringing this problem to our attention.

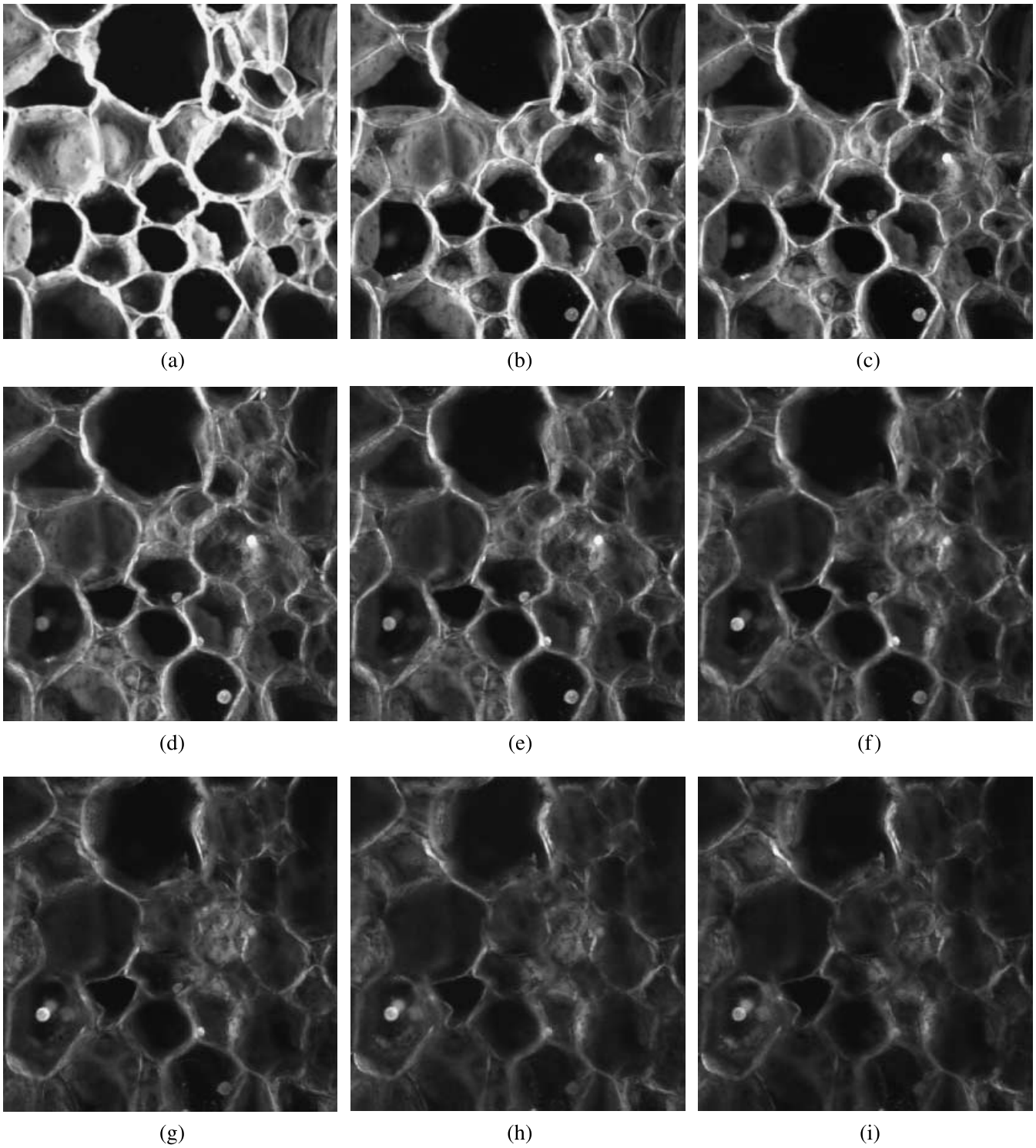

Fig. 9. Some sections from an original CLSM stack of 40 sections: (a) Section # 15, (b) Section # 18, (c) Section # 21, (d) Section # 24, (e) Section # 27, (f) Section # 30, (g) Section # 33, (h) Section # 36, (i) Section # 39.

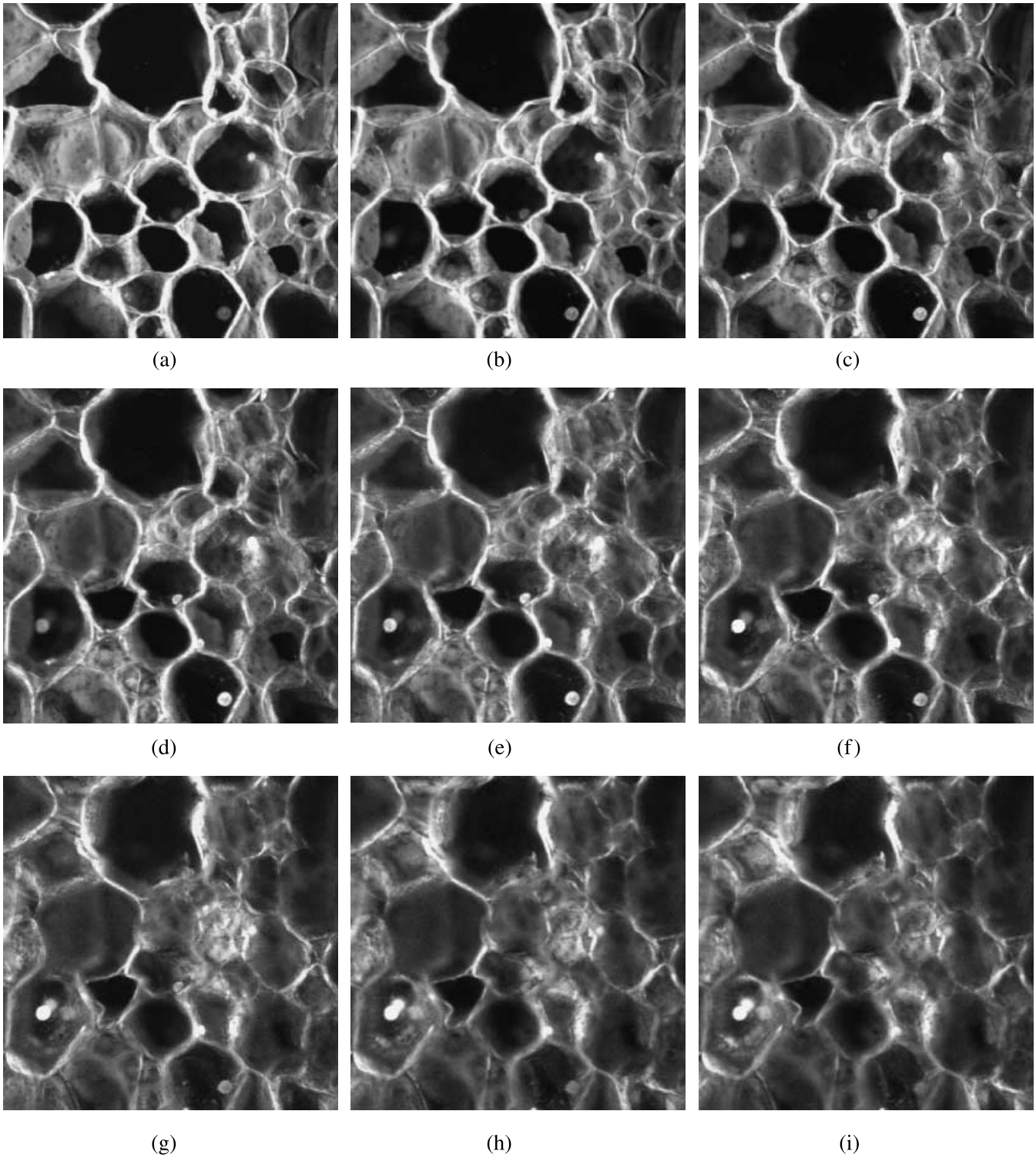

Fig. 10. Some sections from a restored CLSM stack of 40 sections: (a) Section # 15, (b) Section # 18, (c) Section # 21, (d) Section # 24, (e) Section # 27, (f) Section # 30, (g) Section # 33, (h) Section # 36, (i) Section # 39.

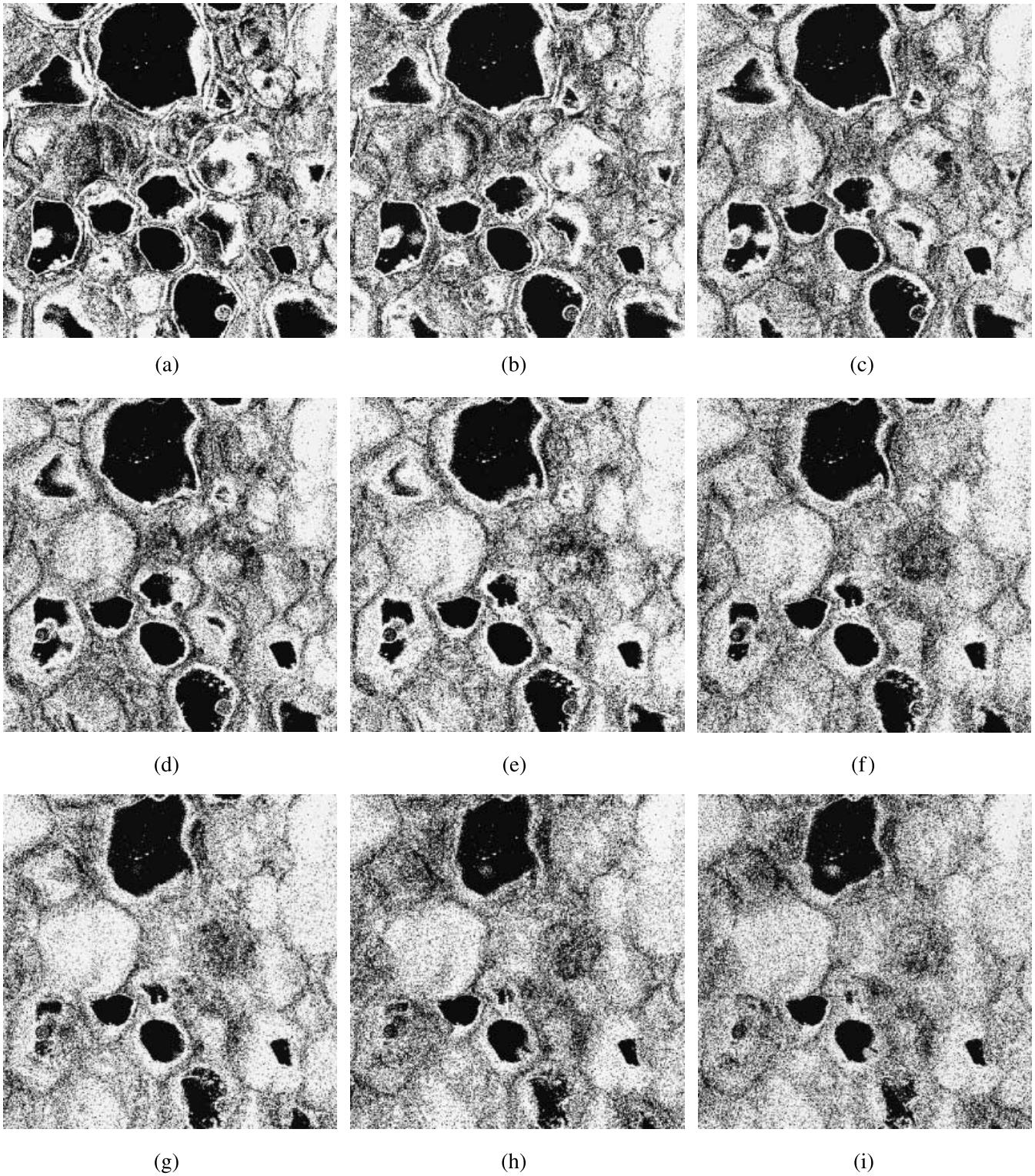

Fig. 11. Detection of outliers (black pixels) for some sections from a restored CLSM stack of 40 sections: (a) Section # 15, (b) Section # 18, (c) Section # 21, (d) Section # 24, (e) Section # 27, (f) Section # 30, (g) Section # 33, (h) Section # 36, (i) Section # 39.

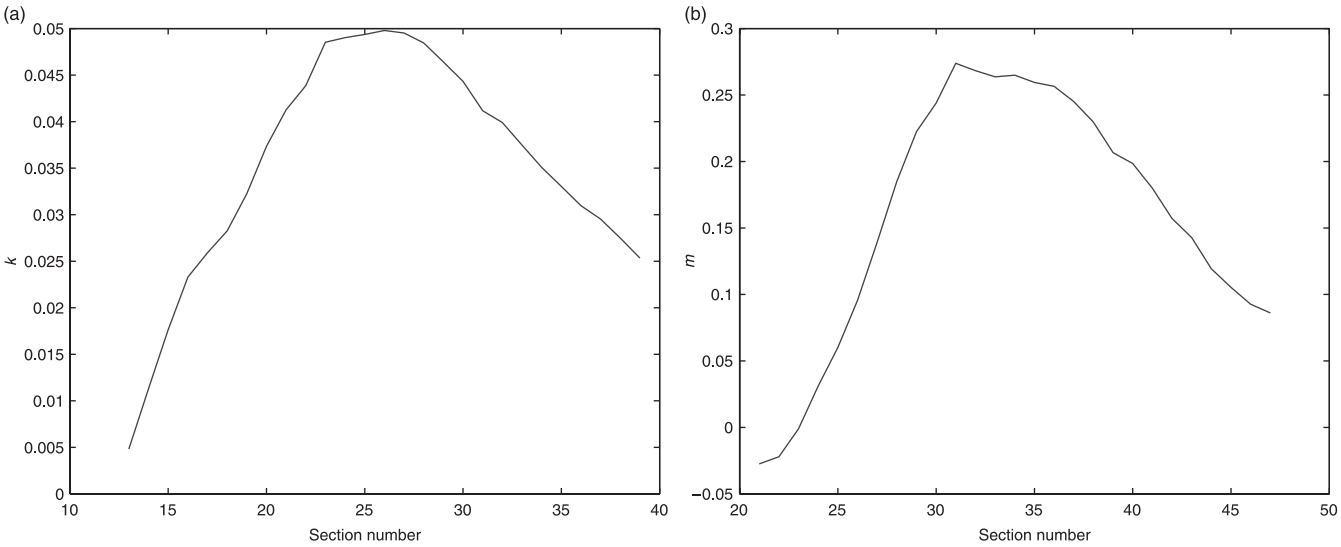

Fig. 12. Plots of attenuation parameters k and m against section number: (a) k against section number, (b) m against section number.

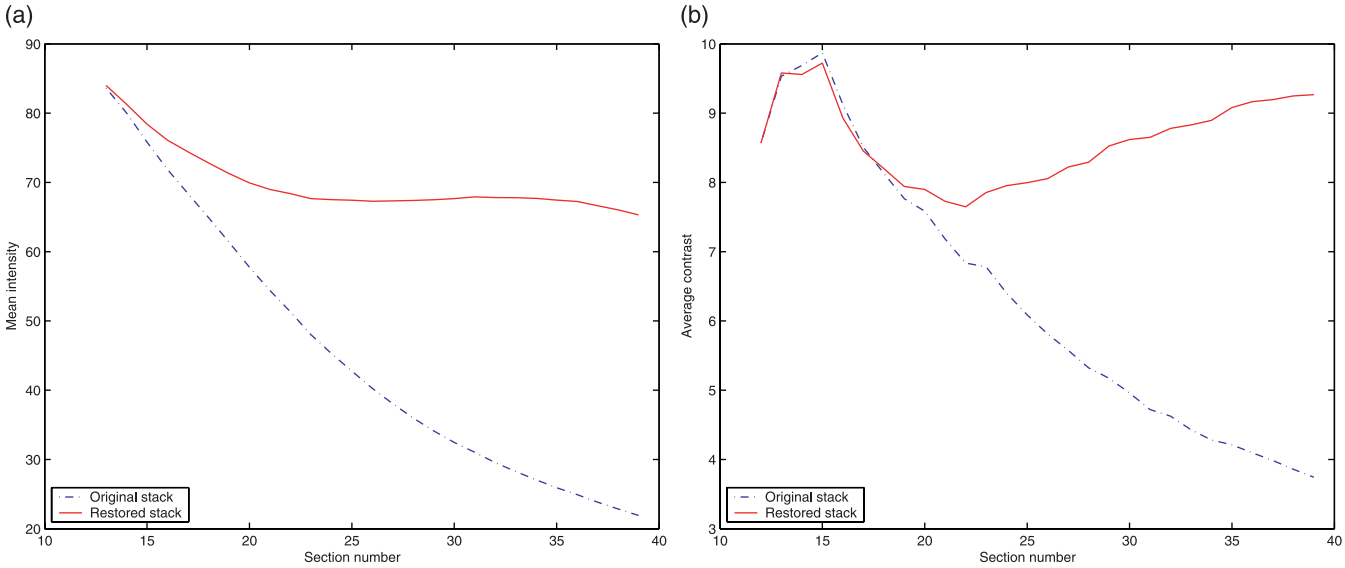

Fig. 13. Plots of the mean intensity and average contrast curves of the original and restored stacks: (a) mean intensity curves, (b) average contrast curves.

References

Black, M. & Anandan, P. (1996) The robust estimation of multiple motions: parametric and piecewise-smooth flow fields. *Comp. Vision Image Understanding*, **63**, 75–104.

Black, M., Sapiro, G., Marimont, D. & Heeger, D. (1998) Robust anisotropic diffusion. *IEEE Trans. Image Processing*, **7**, 421–432.

Black, M. & Rangarajan, A. (1996) On the unification of line processes, outlier rejection, and robust statistics with applications in early vision. *Int. J. Computer Vision*, **19**, 57–92.

Centonze, V. & Pawley, J. (1995) Tutorial on practical confocal microscopy and use of the confocal test specimen. *Handbook of Biological Confocal Microscopy*, 2nd edn (ed. by J. B. Pawley), pp. 549–569. Plenum Press, New York.

Chen, H., Swedlow, J., Grote, M., Sedat, J. & Agard, D. (1995) The collection, processing and display off digital 3d images of biological specimen. *Handbook of Biological Confocal Microscopy*, 2nd edn (ed. by J. B. Pawley), pp. 197–210. Plenum Press, New York.

German, S. & McClure, D. (1987) Statistical methods for tomographic image reconstruction. In *Proc. 46th Session of the Int. Statistical Institute. Bull. ISI*, **52**, 5–21.

Germain, F., Doisy, A., Ronot, X. & Tacqui, P. (1999) Characterization of cell deformation and migration using a parametric estimation of image motion. *IEEE Trans. Biomedical Engineering*, **46**, 584–600.

Ghauharali, R. & Brakenhoff, G. (2000) Fluorescence photobleaching-based image standardization for fluorescence microscopy. *J. Microsc.* **198**, 88–100.

Ghauharali, R., Hofstraat, J. & Brakenhoff, G. (1998) Fluorescence photobleaching-based shading correction for fluorescence microscopy. *J. Microsc.* **192**, 99–113.

Hampel, F., Ronchetti, E., Rousseeuw, P. & Stahel, W. (1986) *Robust Statistics: The Approach Based on Influence Function*. Wiley, New York.

Haussecker, H. & Fleet, D. (2001) Computing optical flow with physical models of brightness variation. *IEEE Trans. Pattern Anal. Mach. Intell.* **23**, 661–673.

Huber, P. (1981) *Robust Statistics*. Wiley, New York.

Irinopoulo, T., Vassy, J., Beil, M., Nicolopoulo, P., Encaoua, D. & Rigaut, J. (1997) 3-D DNA image cytometry by confocal scanning laser microscopy in thick tissue blocks of prostatic lesions. *Cytometry*, **27**, 99–105.

Liljeborg, A., Czader, M. & Porwit, A. (1995) A method to compensate for light attenuation with depth in 3D DNA image cytometry using a confocal scanning laser microscope. *J. Microsc.* **177**, 108–114.

Markham, J. & Conchello, J. (2001) Artefacts in restored images due to intensity loss in 3D fluorescence microscopy. *J. Microsc.* **204**, 93–98.

Meer, P., Mintz, D. & Rosenfeld, A. (1991) Robust regression methods for computer vision. *Int. J. Computer Vision*, **6**, 59–70.

Murray, J. (1998) Evaluating the performance of fluorescence microscopes. *J. Microsc.* **191**, 128–134.

Negahdaripour, S. (1998) Revised definition of optical flow: integration of radiometric and geometric clues for dynamic scene analysis. *IEEE Trans. Pattern Anal. Mach. Intell.* **20**, 961–979.

Nestares, O. & Heeger, D. (2000) Rubust multiresolution alignment of mri brain volumes. *Magnetic Resonance Medicine*, **43**, 705–715.

Odobez, J.M. & Bouthemy, P. (1995) Robust multiresolution estimation of parametric motion models. *J. Visual Communication Image Representation*, **6**, 348–365.

van Oostveldt, P., Verhaegen, F. & Messens, K. (1998) Heterogeneous photobleaching in confocal microscopy caused by differences in refractive index and excitation mode. *Cytometry*, **32**, 137–146.

Ortiz de Solorzano, C., Garcia Rodriguez, E., Jones, A., Pinkel, D., Gray, J., Sudar, D. & Lockett, S. (1999) Segmentation of confocal microscope images of cell nuclei in thick tissue sections. *J. Microsc.* **193**, 212–226.

Pawley, J. (1990) *Handbook of Biological Confocal Microsocopy*. Plenum Press, New York.

Rigaut, J. & Vassy, J. (1991) High-resolution 3D images from confocal scanning laser microscopy: quantitative study and mathematical correction of the effects from bleaching and fluorescence attenuation in depth. *Anal. Quant. Cytol.* **13**, 223–232.

Rodenacker, K., Aubele, P., Hutzler, M. & Umesh Adiga, P. (1997) Groping for quantitative digital 3-D image analysis: an approach to quantitative fluorescence in situ hybridization in thick tissue sections of prostate carcinoma. *Anal. Cell. Pathol.* **15**, 19–29.

Rodenacker, K., Hausner, M., Kuhn, M., Wuertz, S. & Purkayastha, S. (2001) Depth intensity correction of biofilm volume data from confocal laser scanning microscopes. *Image Analysis Stereology*, **20** (Suppl. 1), 556–560.

Roerdink, J. & Bakker, M. (1993) An FFT-based method for attenuation correction in fluorescence confocal microscopy. *J. Microsc.* **169**, 3–14.

Rousseeuw, P. & Leroy, A. (1987) *Robust Regression and Outlier Detection*. Wiley, New York.

Sawhney, H. & Ayer, S. (1996) Compact representations of video through dominant and multiple motion estimation. *IEEE Trans. Pattern Anal. Mach. Intell.* **18**, 814–830.

Tsien, R. & Waggoner, A. (1995) Fluorophores for confocal microscopy. *Handbook of Biological Confocal Microscopy*, 2nd edn (ed. by J. B. Pawley), pp. 267–279. Plenum Press, New York.

Visser, T., Groen, F. & Brakenhoff, G. (1991) Absorption and scattering correction in fluorescence confocal microscopy. *J. Microsc.* **163**, 189–200.